Supporting Information

Photodimerization induced Photomechanical behaviour in Alkyldiammonium Salts of *trans*-Dichlorocinnamates: Exploration of [2+2] Reactions in as Synthesized Salts, Single Crystals and Organogels

Shaheen Sultana, Debasis Pal, Kumar Biradha*

Table of Contents

Experimental Details /Methods

General

All the solvents (SRL chemicals 99.8%), 2,4-/3,4-Dichlorobenzaldehyde (TCI chemicals >95.0%), Malonic acid (Spectrochem >98.0%) 1,2-ethane/1,3-propane/1,4-butanediamine (TCI chemicals >98.0%) were purchased from the respective chemical vendor and used without further purification. NMR spectra were recorded on a Bruker 500 MHz NMR instrument. FT-IR spectra were collected by a PerkinElmer UATR Two spectrometer. Thermogravimetric analysis (TGA) and Differential thermal analysis (DTA) were done under a nitrogen atmosphere at a heating rate of 10 °C/min with a PerkinElmer instrument, Pyris Diamond TG/DTA. The solid-state luminescence spectra were recorded with a Spex Fluorolog-3 (model FL3-22) spectrofluorometer. Optical microscopic images of the solvates were captured with ACUCAL stereo zoom microscope. Single-crystal data were collected on a Bruker D8-Venture X-ray diffractometer that used graphite-monochromated Mo Kα radiation (λ = 0.71073 A) by the hemisphere method. The structures were solved by direct methods and refined by the least-squares method on F^2 using SHELXL-2018/3. Non-hydrogen atoms were refined anisotropically, and hydrogen atoms were fixed at calculated positions and refined by using a riding model. The PXRD patterns were collected in Bragg−Brentano mode using a D8-Advance A-25 diffractometer (Cu Kα1 radiation, λ=1.54060 A) at ambient conditions (T = 298 K). FESEM images of the crystals were recorded by using field emission scanning electron microscope, Gemini ZEISS SUPRA-40, Model no. 2593 with oxford EDS detector. X-ray photoelectron spectroscopy (XPS) was performed using ESCALAB Xi, Thermo-Scientific, UK, with a monochromatic Al Kα X-ray source (1486.6 eV). The CAE (constant analyzer energy) for survey spectra is 100 eV and that for high-resolution spectra is 50 eV. AFM images were taken using Agilent Technology, Nanonics Type-020-525028 AFM instrument. MALDI-TOF experiments were performed using a BRUKER ULTRAFLEXTREME MALDI TOF/TOF mass spectrometer using 2,5-dihydroxybenzoic acid as the matrix. Nanoindentation was performed using TI 950 TriboIndenter, Hysitron Inc.

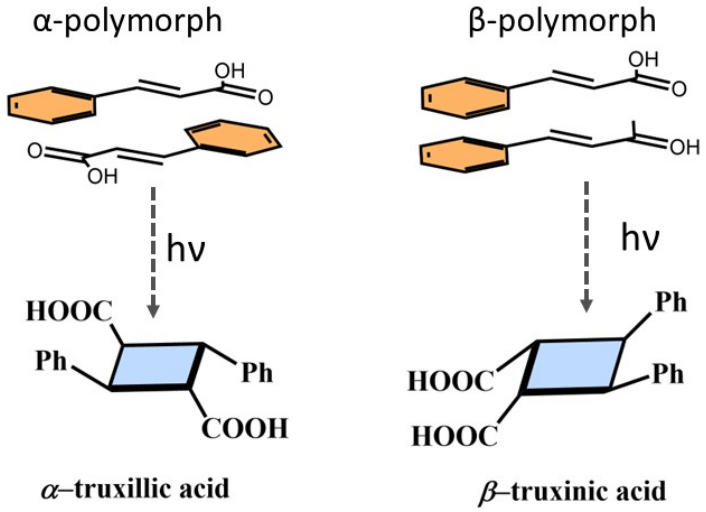

Scheme S1. Illustration of crystal packing and [2+2] reactivity in the polymorph of cinnamic acid.

Synthesis and Characterization

All the salts were synthesized by reacting the alkyl diamines (H_2N-$(CH_2)_n$-NH_2, *n*= 2-4) with corresponding monocarboxylic acids; *trans*-2,4/3,4-dichlorocinnamic acid in 1:2 molar ratio in methanol. All the salts prepared were characterized by FTIR, ^{1}H-NMR, and single crystal x-ray diffraction in few cases.

$B_2(A_{24})_2$: ^{1}H NMR (400 MHz, DMSO-d_6): δ = 7.85-7.83 (d, J = 8Hz, 1H), 7.67 (s, 1H), 7.60-7.56 (d, J =16Hz, 1H), 7.44-7.42 (d, J = 8Hz, 1H), 6.58-6.54 (d, J = 16Hz, 1H), 3.64 (m, 3H), 2.83 (m, 2H). FT-IR (KBr pellet): 3029, 2924, 1645, 1546, 1500, 1466, 1392, 1373, 1334, 1272, 1195, 1102, 1067, 1044, 971, 859, 835, 816, 770, 700, 658, 557 cm^{-1}.

$B_2(A_{34})_2$: ^{1}H NMR (400 MHz, DMSO-d_6): δ = 7.91-7.89 (d, J = 8Hz, 1H), 7.63-7.61 (d, J = 8Hz, 2H), 7.33-7.29 (d, J =16Hz, 1H), 6.60-6.56 (d, J = 16Hz, 1H), 3.63 (m, 2H), 2.83 (m, 2H). FT-IR (KBr pellet): 2572, 2208, 1649, 1554, 1505, 1481, 1399, 1369, 1285, 1236, 1195, 1138, 1032, 1008, 984, 918, 869, 829, 763, 737, 693, 570, 538, 513 cm^{-1}.

$B_3(A_{24})_2$: ^{1}H NMR (400 MHz, DMSO-d_6): δ = 7.83-7.82 (d, J = 8Hz, 1H), 7.66 (s, 1H), 7.54-7.51 (d, J =12Hz, 1H), 7.43-7.41 (d, J = 8Hz, 1H), 6.54-6.51 (d, J = 12Hz, 1H), 2.83 (t, 2H), 1.78 (t, 1H). FT-IR (KBr pellet): 2944, 2937, 1646, 1592, 1552, 1503, 1470, 1356, 1274, 1136, 1095, 1046, 973, 875, 818, 761, 696, 655, 557 cm^{-1}.

$B_3(A_{34})_2$: ^{1}H NMR (400 MHz, DMSO-d_6): δ = 7.82-7.81 (d, J = 4Hz, 1H), 7.59-7.57 (d, J = 8Hz, 1H), 7.55-7.53 (d, J =8Hz, 1H), 7.22-7.18 (d, J = 16Hz, 1H), 6.54-6.50 (d, J = 16Hz, 1H), 2.84 (t,

2H), 1.80 (m, 1H). FT-IR (KBr pellet): 2921, 2840, 1647, 1551, 1514, 1502, 1470, 1402, 1378, 1282, 1233, 1209, 1143, 1136, 1030, 981, 905, 857, 819, 753, 686, 584, 505 cm^{-1}.

$B_4(A_{24})_2$: ^1H NMR (400 MHz, DMSO-d_6): δ = 7.95-7.94 (d, J = 4Hz, 1H), 7.80-7.77 (d, J =12Hz 1H), 7.71-7.70 (d, J =4Hz, 1H), 7.48-7.45 (dd, J = 4Hz, 1H), 6.64-6.61 (d, J = 12Hz, 1H), 2.79 (m, 2H), 1.57 (m, 2H). FT-IR (KBr pellet): 2995, 2945, 2874, 1638, 1583, 1532, 1472, 1370, 1292, 1268, 1138, 1093, 1063, 1045, 970, 892, 863, 829, 764, 743, 691, 657, 558, 506 cm^{-1}.

$B_4(A_{34})_2$: ^1H NMR (400 MHz, DMSO-d_6): δ = 8.01 (s, 1H), 7.72-7.64 (q, 1H), 7.58-7.54 (d, J =16Hz, 1H), 6.66-6.62 (d, J = 16Hz, 1H), 6.03 (m, 3H), 2.82 (m, 2H), 1.59 (m, 2H). FT-IR (KBr pellet): 3039, 2982, 1650, 1609, 1523, 1470, 1446, 1387, 1366, 1290, 1269, 1233, 1192, 1131, 1066, 1029, 968, 890, 862, 821, 760, 683, 560, 532, 503 cm^{-1}.

Compounds	**$B_2(A_{24})_2$**	**$B_3(A_{24})_2$**	**$B_4(A_{24})_2$**	**$B_4(A_{34})_2$**	***d*-$B_2(A_{24})_2$**	***d*-$B_2(A_{34})_2$**
Formula	$C_{20}H_{20}Cl_4N_2O_6$	$C_{21}H_{16}Cl_4N_2O_4$	$C_{11}H_{12}Cl_2NO_2$	$C_{11}H_{12}Cl_2NO_2$	$C_{20}H_{20}Cl_4N_2O_4$	$C_{20}H_{20}Cl_4N_2O_4$
CCDC	**2533551**	**2533552**	**2533556**	**2533553**	**2533555**	**2533554**
Mol. Wt.	526.18	502.16	261.12	261.12	494.18	494.18
T (K)	306	300	304	303	301	303
System	monoclinic	orthorhombic	triclinic	triclinic	monoclinic	monoclinic
Space group	$P2_1/c$	*Pbca*	*P*-1	*P*-1	$P2_1/c$	$P2_1/c$
a (Å)	7.739(2)	8.365(10)	6.7040(8)	7.2940(11)	19.923(2)	20.664(6)
b (Å)	38.409(11)	13.846(18)	8.4116(10)	7.3566(10)	7.8306(8)	7.984(2)
c (Å)	8.028(3)	41.35(5)	11.5801(13)	11.7557(19)	14.0052(13)	13.230(4)
α (º)	90	90	71.576(7)	88.446(5)	90	90
β (º)	91.796(10)	90	80.805(7)	84.280(5)	99.688(3)	102.428(9)
γ (º)	90	90	79.641(8)	72.170(4)	90	90
V (A^3)	2385.1(13)	4789(10)	605.73(13)	597.51(16)	2153.8(4)	2131.7(10)
Z	4	8	2	2	4	4
D (g/cm^3)	1.465	1.393	1.432	1.450	1.524	1.540
$R_1[I > 2\sigma(I)]$	0.1044	0.0704	0.0522	0.0663	0.0579	0.0585
wR_2(on F^2, all data)	0.2608	0.2484	0.1910	0.1966	0.1887	0.1905

Table S1. Crystallographic parameters.

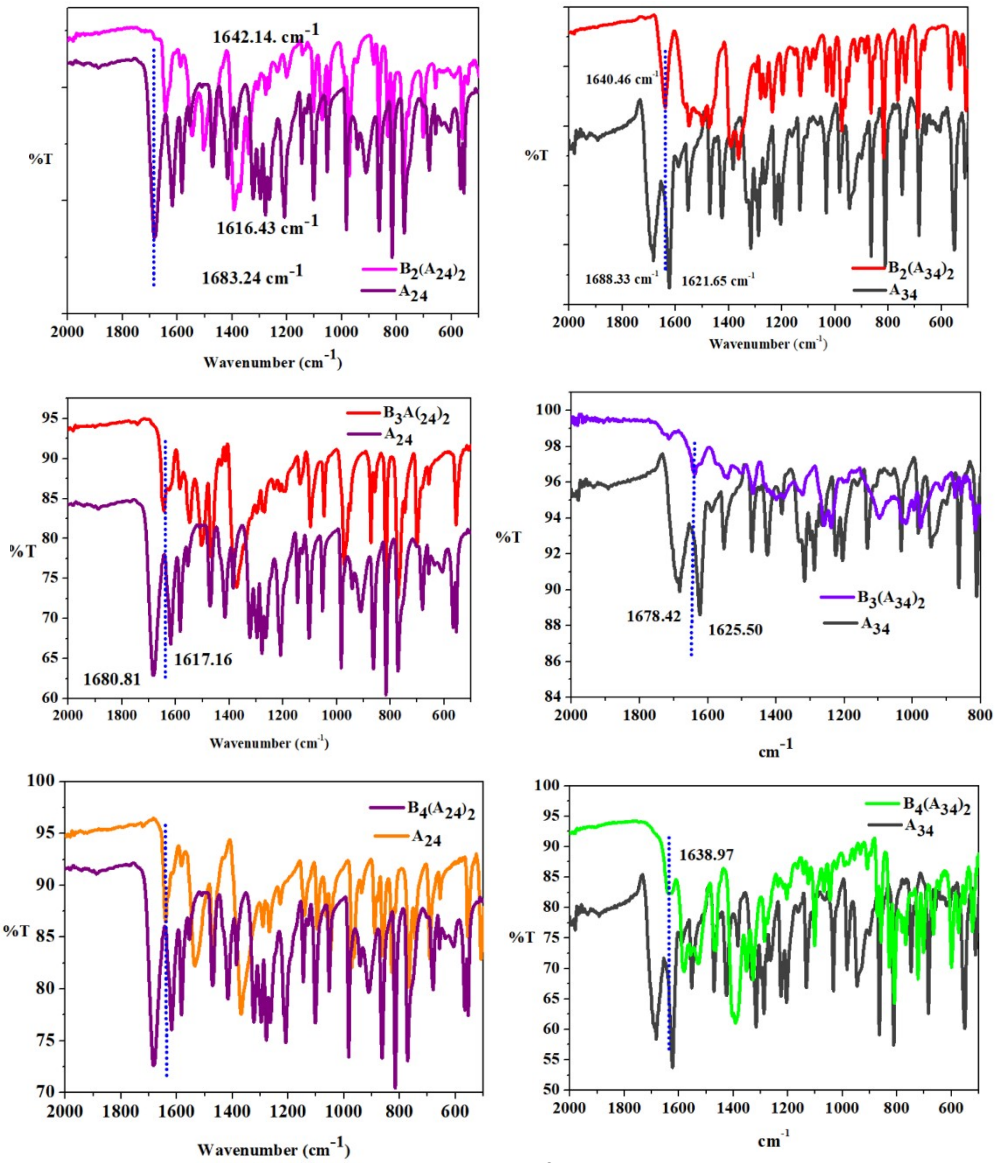

Figure S1 FTIR spectra confirming ammonium salts formation.

PXRD analysis:

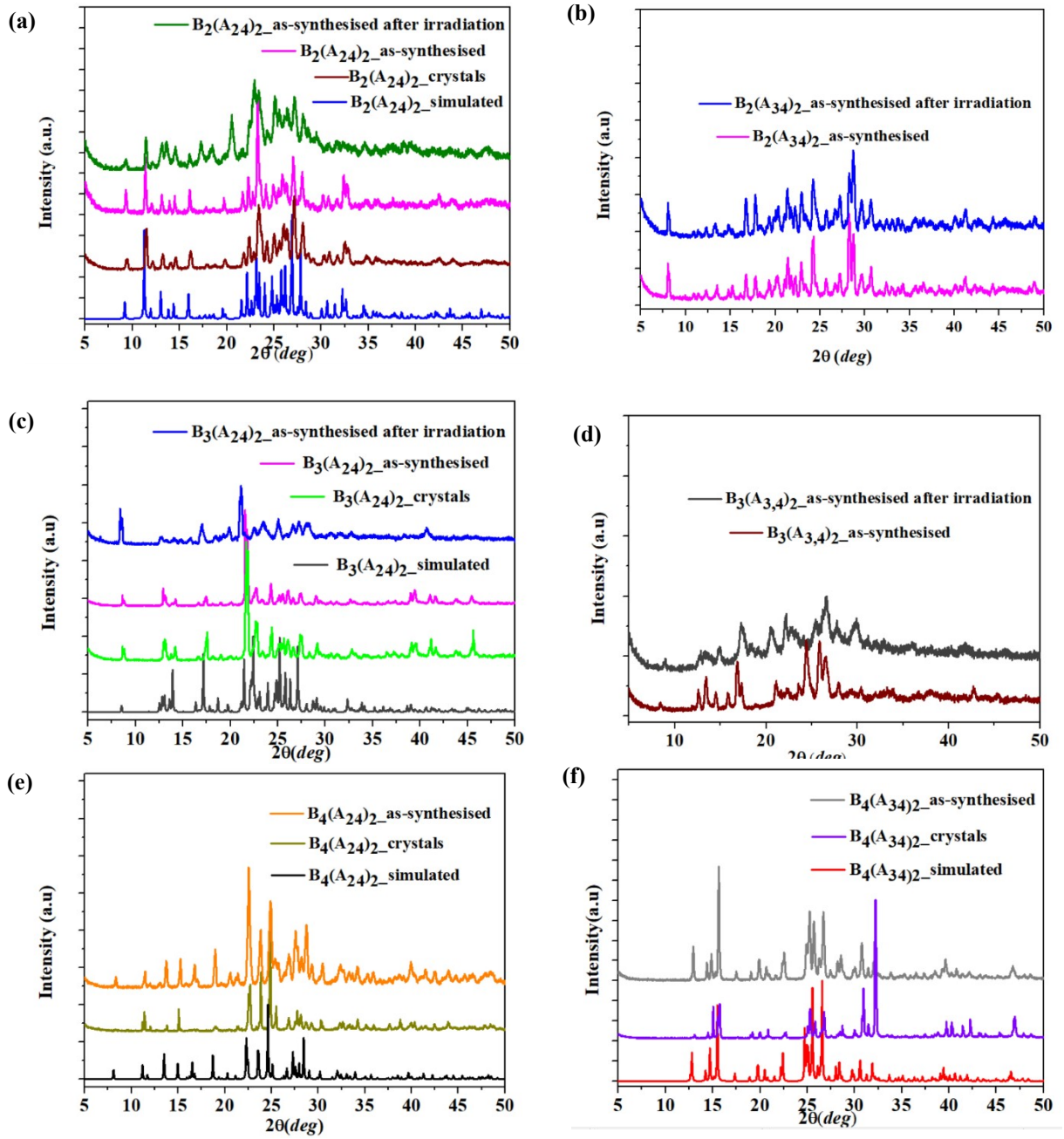

Figure S2 PXRD analysis of as-synthesised salts with their single crystals grown. PXRD pattern after irradiation are given for B_2 and B_3 salts.

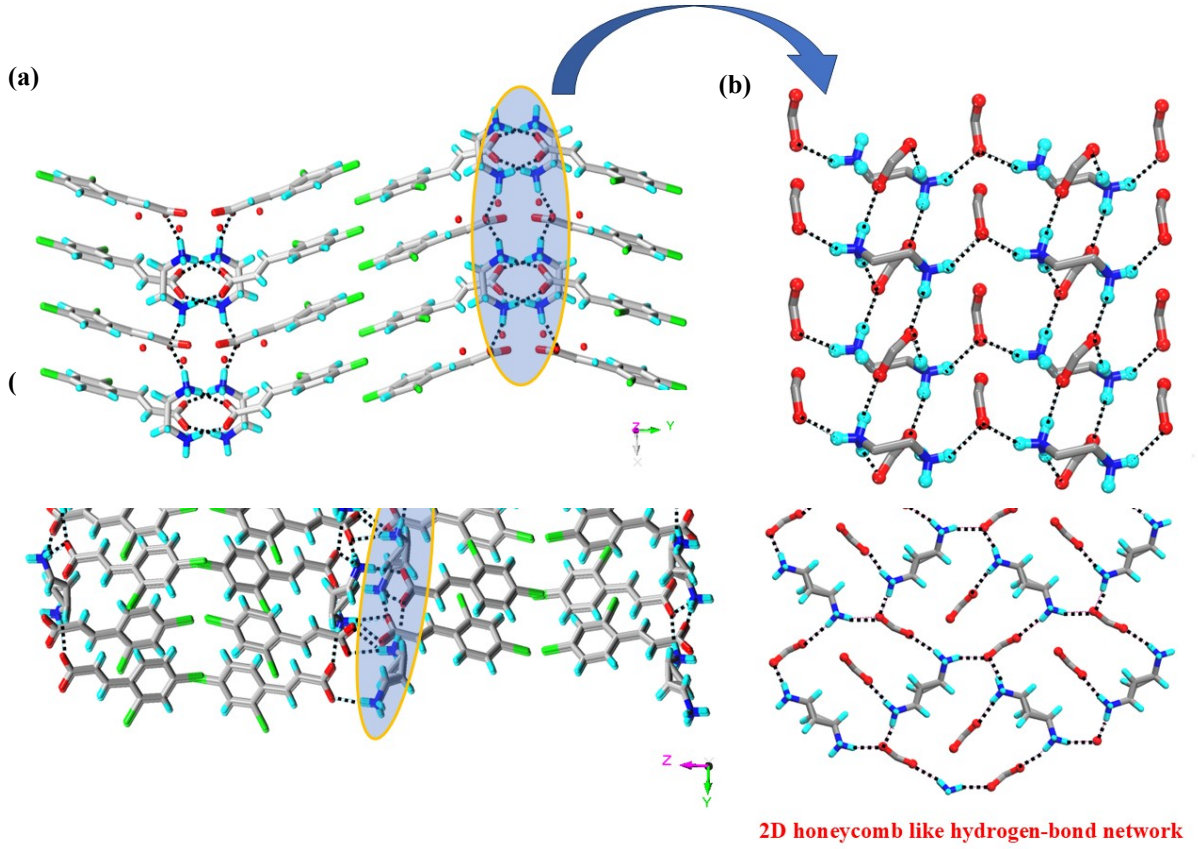

Figure S3 Crystal structure illustration of $B_2(A_{24})_2$ and $B_3(A_{24})_2$ respectively; (a, c) overall 3D structure, (b, d) 2D hydrogen bonded layer.

Table S3 Hydrogen bonding geometry in $B_n(A_{m4})_2$ salts.

Compound	Type	H···A (Å)	D···A (Å)	D-H···A (°)
$B_2(A_{24})_2$	N(1)-H(1A)···O(1A)	1.93	2.808(7)	170
	N(1)-H(1A)···O(2A)	2.51	3.187(7)	133
	N(1)-H(1B)···O(2B)	2.05	2.848(7)	149
	N(1)-H(1C)···O(1A)	1.94	2.810(7)	166
	N(2)-H(2A)···O(1A)	2.58	3.203(7)	128
	N(2)-H(2A)···O(1A)	1.99	2.872(7)	173
	N(2)-H(2B)···O(2B)	2.02	2.791(6)	144
	N(2)-H(2C)···O(2A)	1.88	2.765(6)	172
	C(7A)-H(7A)···Cl(1A)	2.74	3.070(7)	102

	C(7B)-H(7B)···Cl(1B)	2.62	3.031(7)	108
$B_3(A_{24})_2$	N(1)-H(1A)···O(3)	1.86	2.711(7)	159
	N(2)-H(2A)···O(3)	1.96	2.833(7)	166
	N(2)-H(2A)···O(4)	2.43	3.121(7)	135
	N(2)-H(2B)···O(2)	1.96	2.809(7)	159
	N(2)-H(2C)···O(1)	2.08	2.951(7)	165
	N(2)-H(2C)···O(4)	2.54	2.858(7)	102
	C(3)-H(3)···Cl(1)	2.60	3.054(7)	111
	C(12)-H(12)···Cl(3)	2.63	3.077(7)	110
d-$B_2(A_{24})_2$	N(1)-H(1A)···O(3)	2.09	2.882(4)	148
	N(1)-H(1A)···O(4)	2.48	3.300(4)	153
	N(1)-H(1B)···O(2)	1.95	2.759(4)	150
	N(1)-H(1C)···O(3)	1.97	2.851(4)	169
	N(2)-H(2A)···O(4)	2.00	2.882(4)	172
	N(2)-H(2B)···O(4)	2.02	2.879(4)	163
	N(2)-H(2C)···O(1)	1.90	2.746(4)	157
	C(13)-H(13)···Cl(1)	2.60	3.119(4)	114
	C(13)-H(13)···O(3)	2.46	2.878(4)	105
	C(19)-H(19B)···O(2)	2.60	3.240(4)	124
	C(20)-H(20B)···O(1)	2.42	3.187(5)	135
d-$B_3(A_{24})_2$	N(1)-H(1A)···O(2)	1.89	2.737(4)	159
	N(1)-H(1B)···O(4)	1.98	2.834(4)	160
	N(1)-H(1C)···O(4)	2.06	2.943(4)	174
	N(2)-H(2A)···O(3)	1.92	2.769(4)	159
	N(2)-H(2B)···O(1)	1.88	2.745(4)	163
	N(2)-H(2B)···O(2)	2.53	2.974(4)	112

	N(2)-H(2C)···O(3)	2.52	3.179(4)	131
	N(2)-H(2C)···O(4)	2.09	2.975(4)	172
	C(11)-H(11)···O(3)	2.54	2.912(5)	102
	C(19)-H(19A)···O(1)	2.53	3.262(4)	133
$B_4(A_{24})_2$	N(1)-H(1A)···O(2)	2.00	2.829(3)	155
	N(1)-H(1B)···O(2)	1.92	2.771(3)	158
	N(1)-H(1C)···O(1)	1.85	2.736(3)	174
	C(2)-H(2)···Cl(1)	2.64	3.068(3)	109
	C(2)-H(2)···O(1)	2.53	2.840(3)	100
	C(8)-H(8)···O(2)	2.46	3.362(3)	164
	C(10)-H(10B)···Cl(2)	2.92	3.682	136
$B_4(A_{34})_2$	N(1)-H(1A)···O(1)	1.91	2.787(3)	168
	N(1)-H(1A)···O(2)	2.59	3.286(3)	135
	N(1)-H(1B)···O(1)	2.01	2.771(4)	143
	N(1)-H(1C)···O(2)	1.88	2.749(4)	166
	C(7)-H(7)···O(1)	2.53	2.848(4)	100
	C(10)-H(10B)···Cl(1)	2.97	3.804	145

Table S3. List of Cl···Cl interactions parameters.

Compound	Cl···Cl (Å)	<C-Cl···Cl (Å)	Type of Cl···Cl
$\mathbf{B_2(A_{24})_2}$	3.970	150, 93	Type-II
$\mathbf{B_3(A_{24})_2}$	3.721	103, 82	Type-II
***d*-$\mathbf{B_2(A_{24})_2}$**	4.055 4.095	101, 68 134, 134	Type-II Type-I
***d*-$\mathbf{B_2(A_{34})_2}$**	3.660 3.993	125, 125 115, 66	Type-I Type-II

Table S4 Gelation Data.

Solvents / Salts	DMSO	H_2O	DMSO-H_2O(1:1)	Ph-NO_2
$B_2(A_{24})_2$	G (12)†	TS	G (10)	G (20)
$B_2(A_{34})_2$	G (15)	TS	G (10)	WG
$B_3(A_{24})_2$	WG	TS	G (10)	WG
$B_3(A_{34})_2$	WG	TS	G (10)	WG

G = gel († CGC in mg ml^{-1}); TS = turbid solution; WG = weak gel

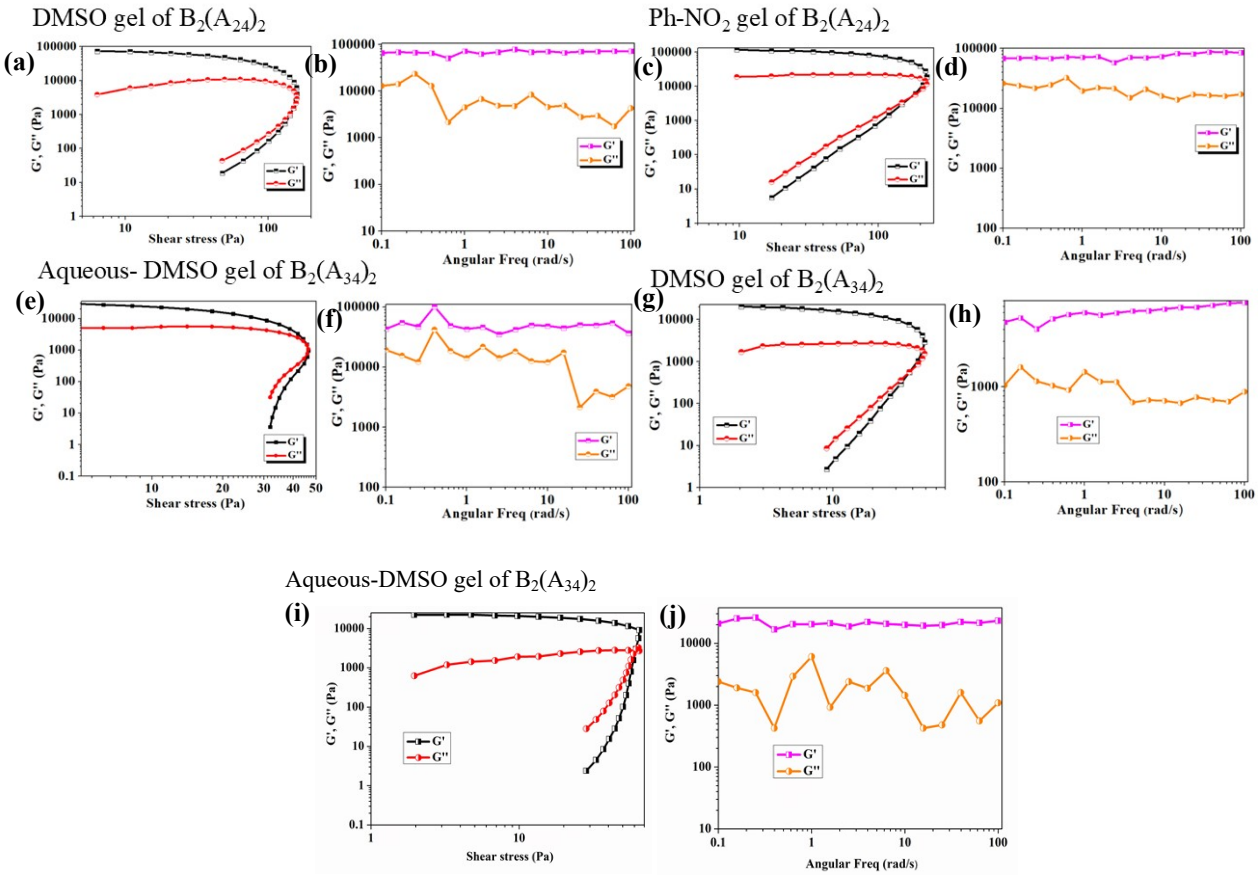

Figure S4 Illustration of the rheological analyses of organogels: variation of storage modulus (G') and loss modulus (G''), (a,c,e,g,i,k) with shear stress; (b,d,f,h,j,l) with frequency.

FESEM images

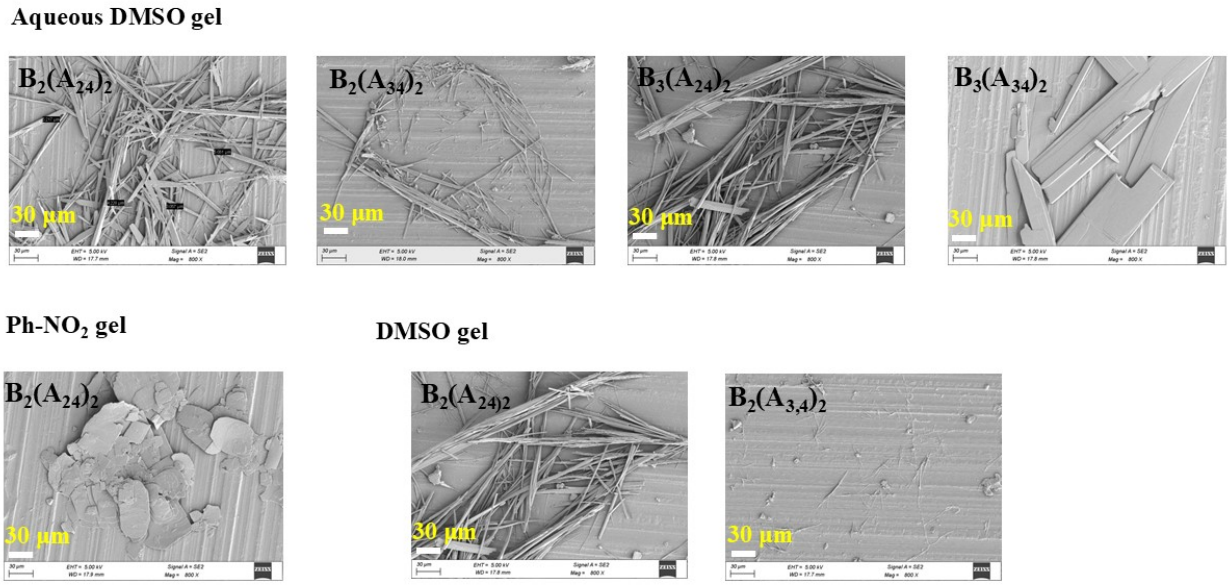

Figure S5 FESEM images showing different morphologies (popsicle stick or plate shaped) for organogels.

PXRD analysis

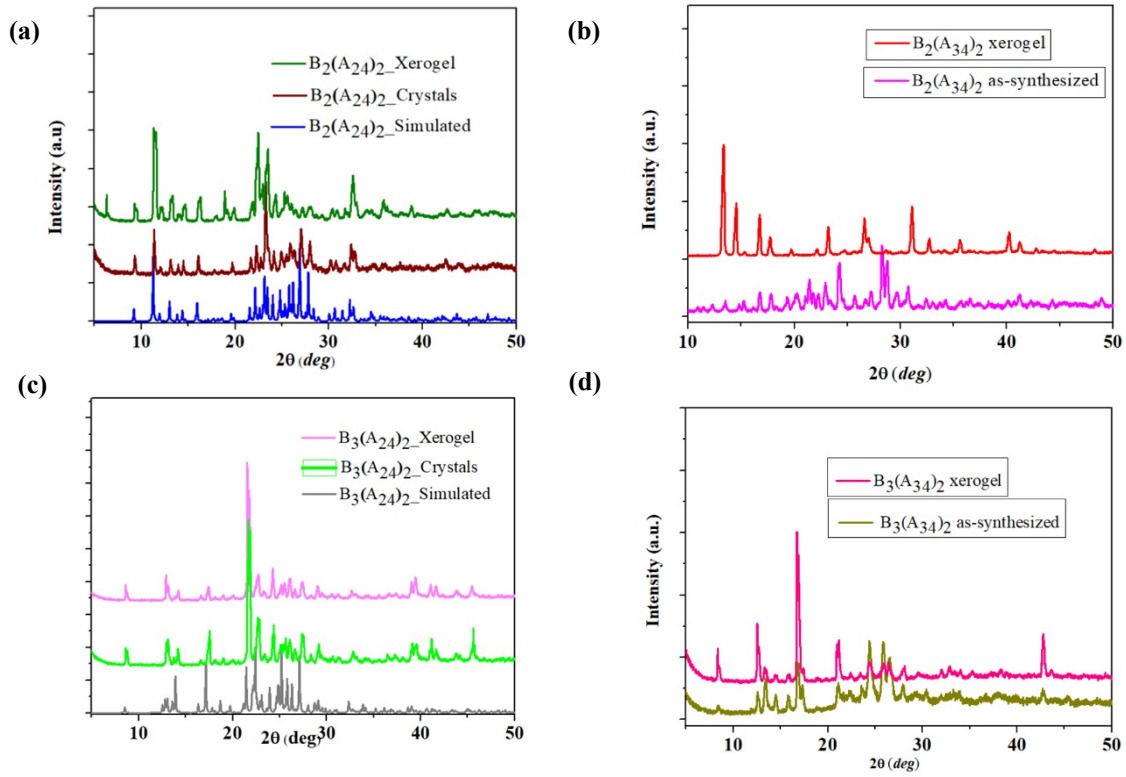

Figure S6 PXRD analysis of crystals and xerogel from aqueous DMSO gel of B_2 and B_3 salts.

^{1}H-NMR Spectra

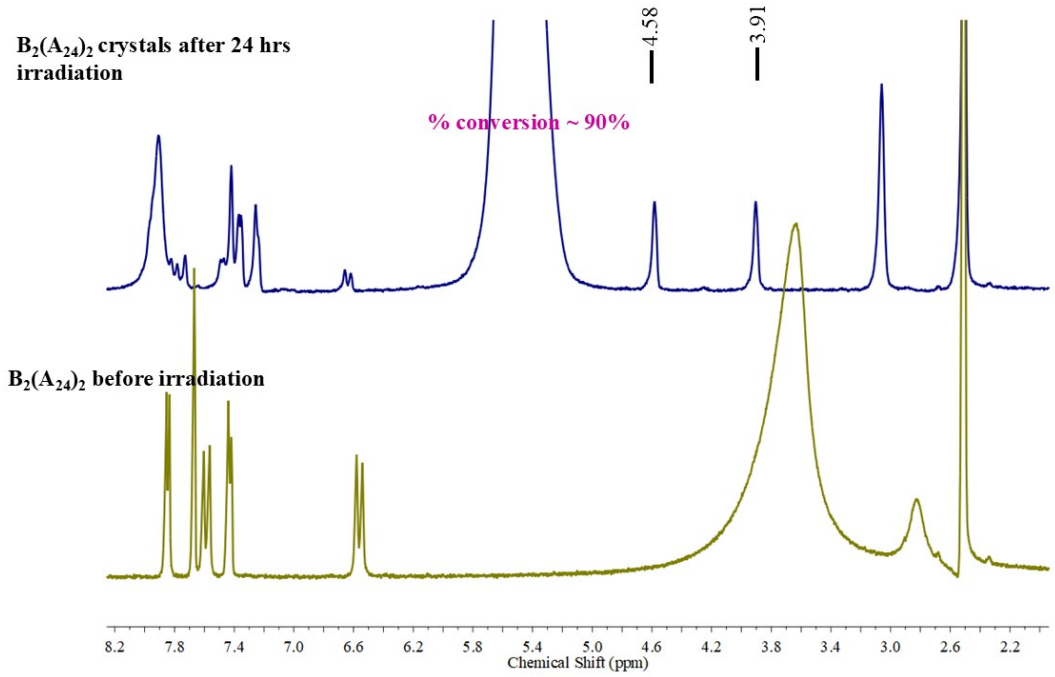

Figure S7 ^{1}H NMR spectra for $B_2(A_{24})_2$ before and after 24 hrs of 365 nm UV irradiation (400MHz, DMSO-d_6).

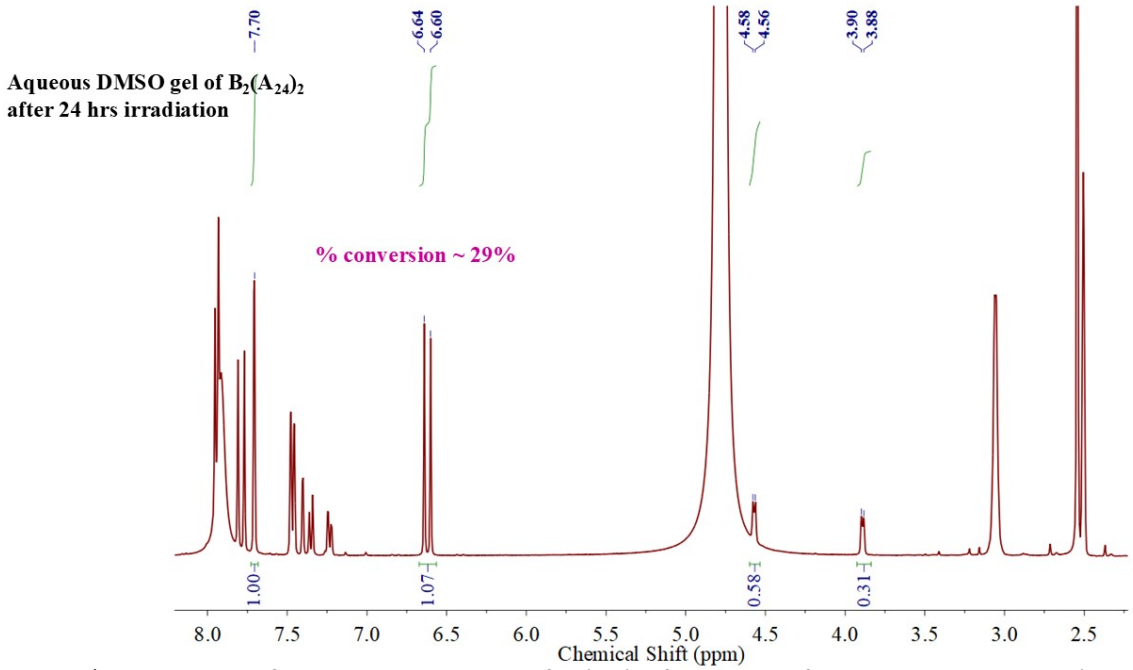

Figure S8 ^{1}HNMR spectra for aqueous DMSO gel of $B_2(A_{24})_2$ after 24 hrs of 365 nm UV irradiation (400MHz, DMSO-d_6).

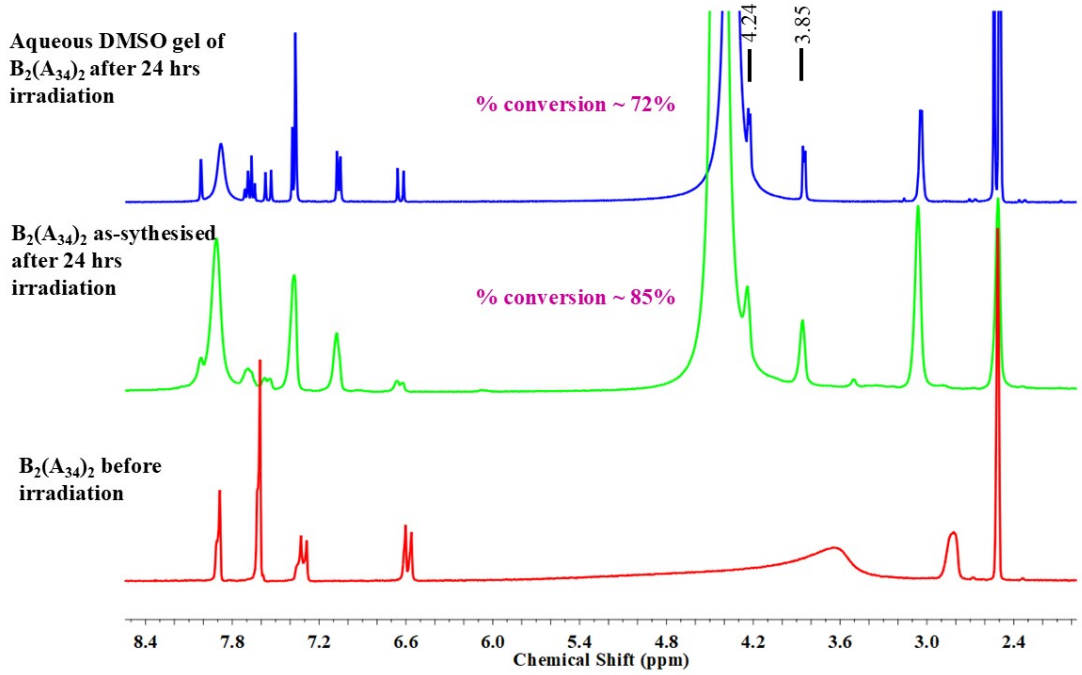

Figure S9 ^{1}HNMR spectra for $B_2(A_{34})_2$ in crystal and organogel state before and after 24 hrs of 365 nm UV irradiation (400MHz, DMSO-d_6).

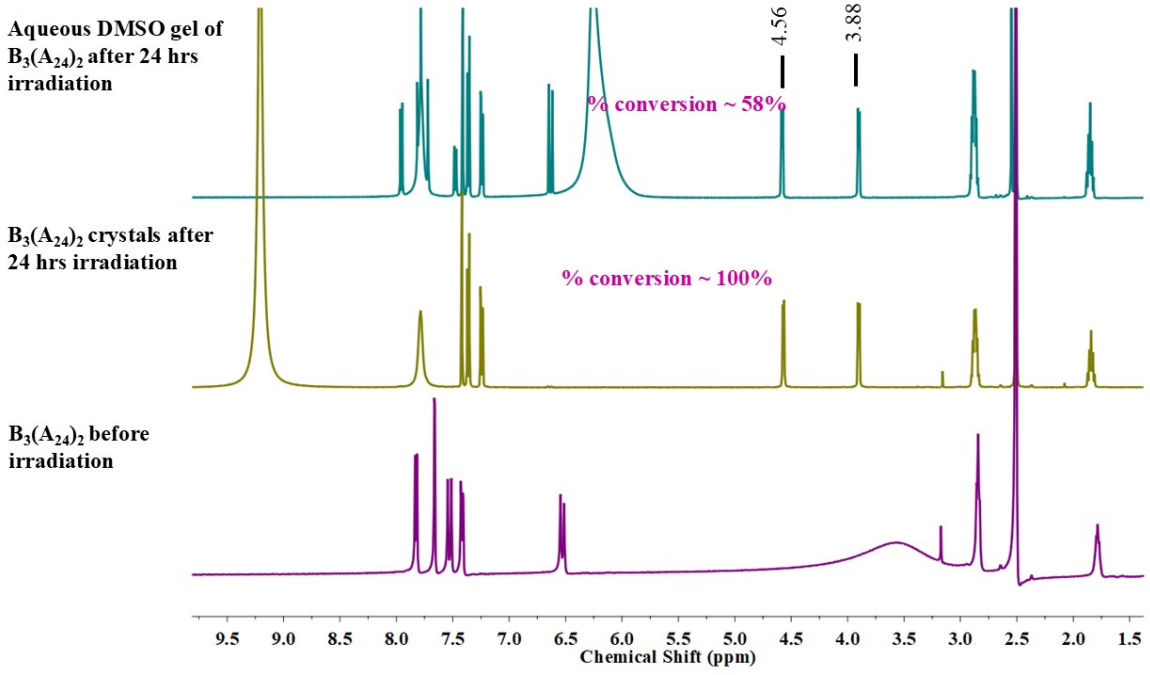

Figure S10 ^{1}HNMR spectra for $B_3(A_{24})_2$ in crystal and organogel state before and after 24 hrs of 365 nm UV irradiation (400MHz, DMSO-d_6).

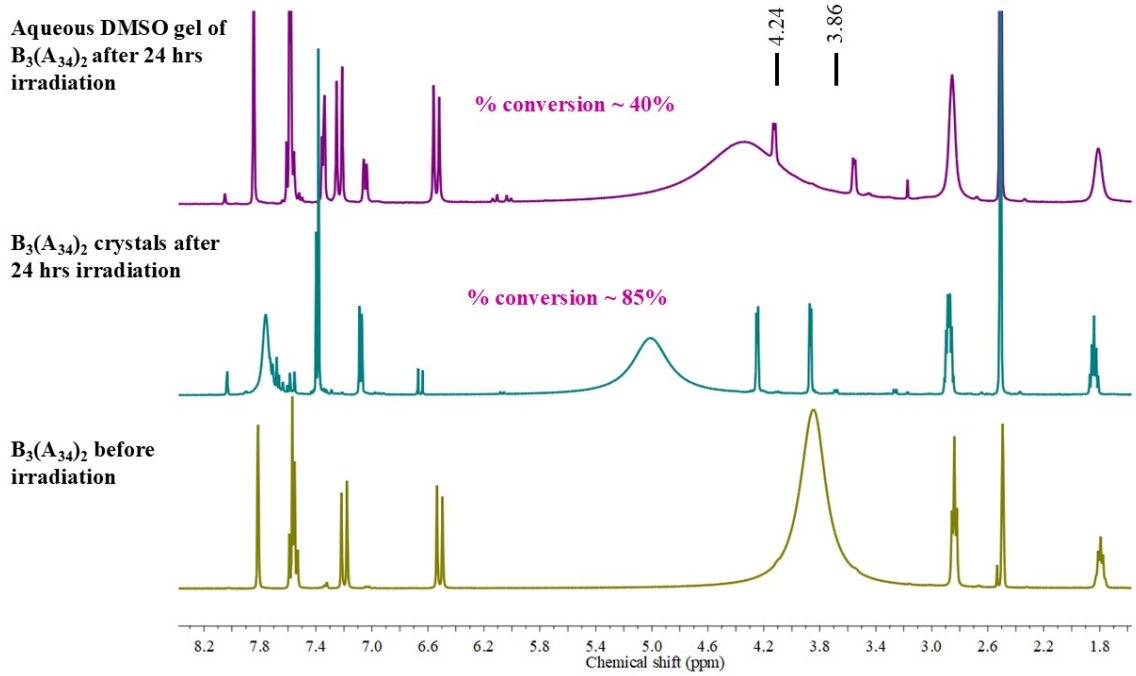

Figure S11 ^{1}HNMR spectra for $B_3(A_{34})_2$ in crystal and organogel state before and after 24 hrs of 365 nm UV irradiation (400MHz, DMSO-d_6).

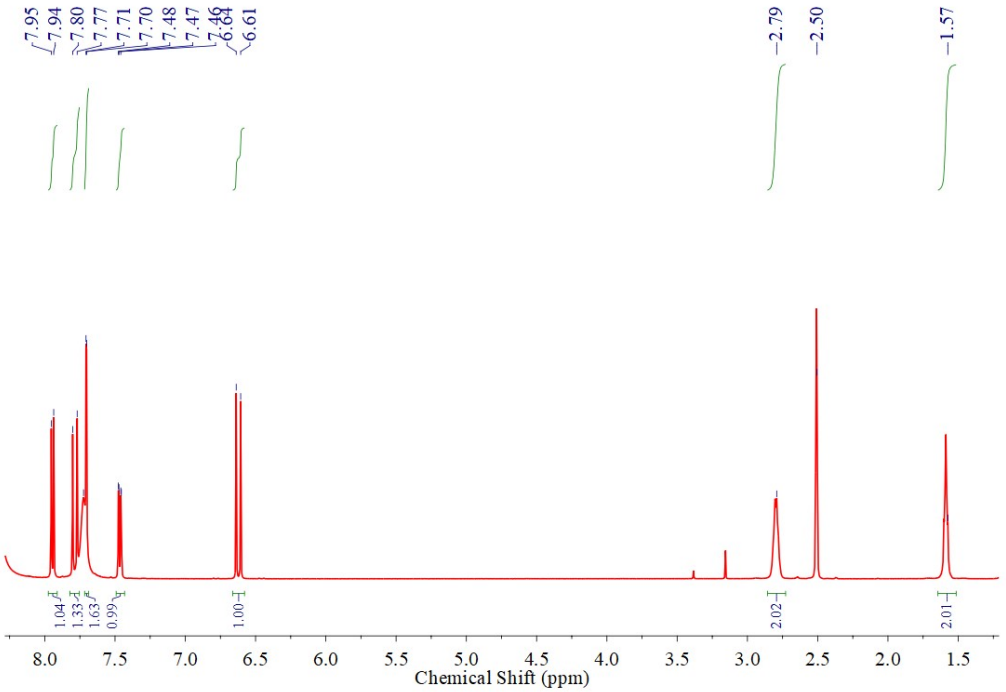

Figure S12 ^{1}HNMR spectrum for $B_4(A_{24})_2$ (400MHz, DMSO-d_6).

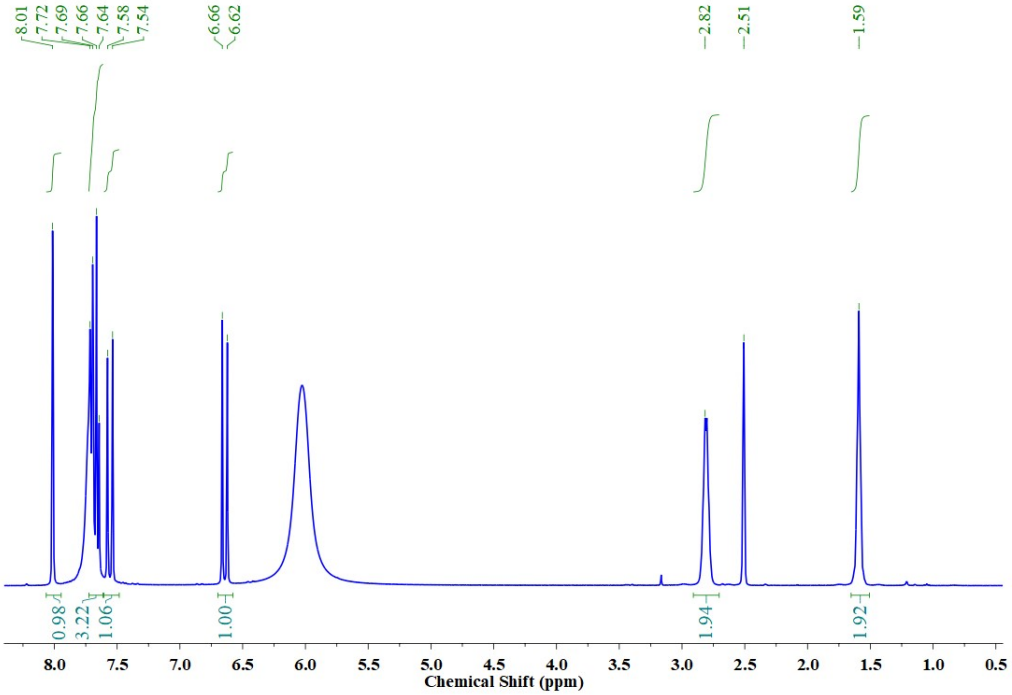

Figure S13 ^{1}HNMR spectrum for $B_4(A_{34})_2$ (400MHz, DMSO-d_6).

MALDI-ToF analysis

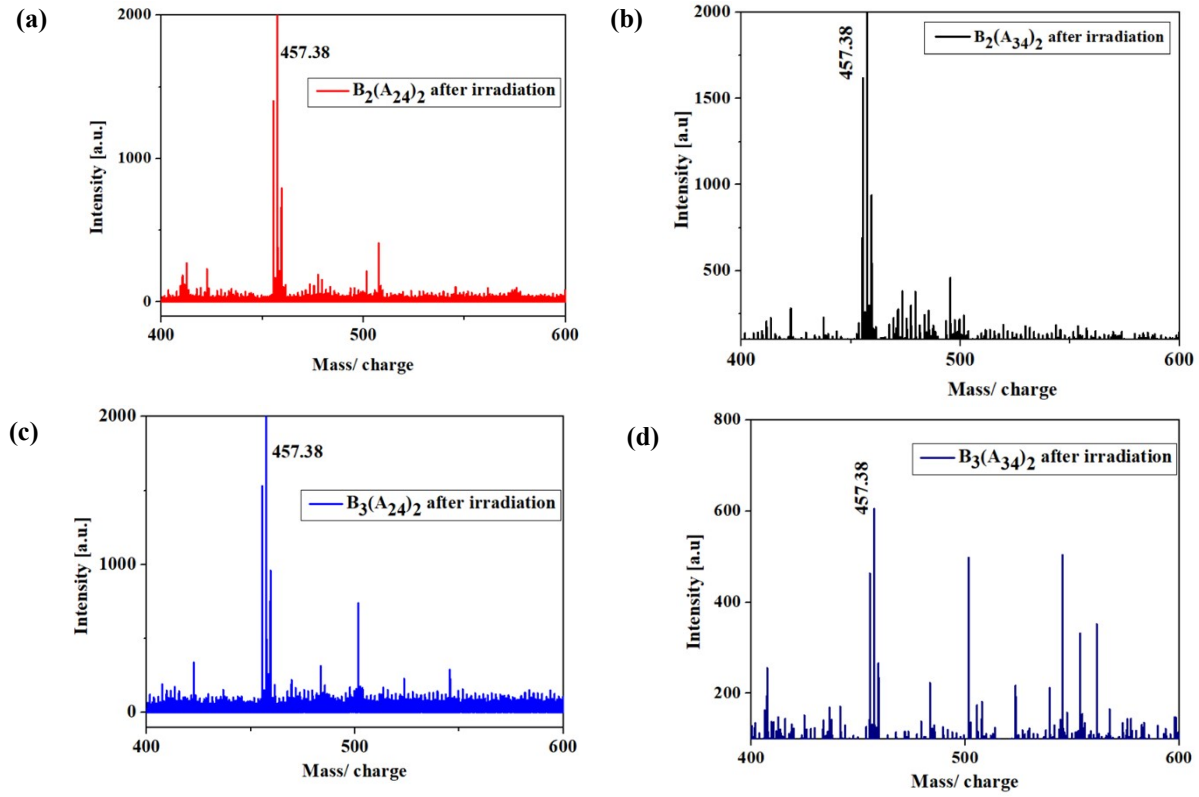

Figure S14 MALDI-ToF analysis after photoirradiation of various salts.

Optical Microscope image

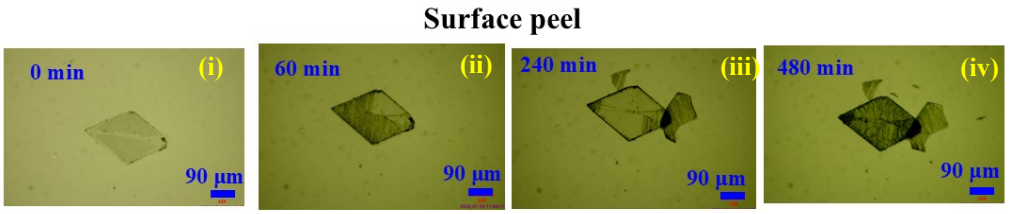

Figure S15 Optical microscopic images of $B_3(A_{24})_2$ crystal at different time intervals indicating surface peeling effect.

FESEM images:

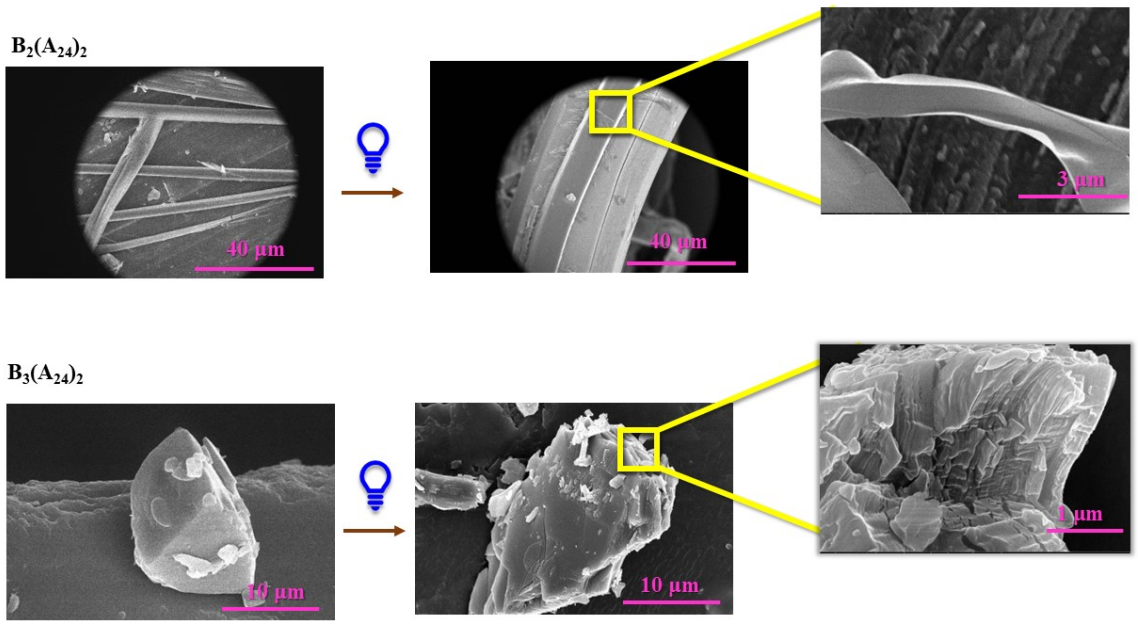

Figure S16 FESEM images indicating (a) bending in $B_2(A_{24})_2$ and (b) development of cracks in $B_3(A_{24})_2$.

AFM images:

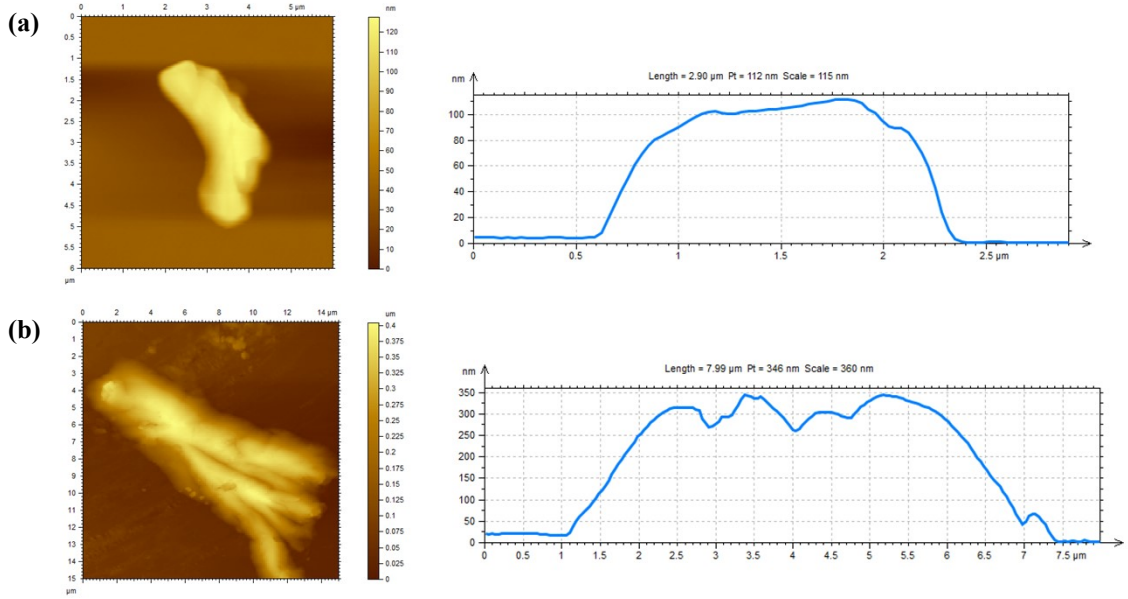

Figure S17 AFM images and height profile of $B_3(A_{24})_2$ from left to right for (a) before and (b) after irradiation.

p-h curve

(a)

$B_2(A_{24})_2$

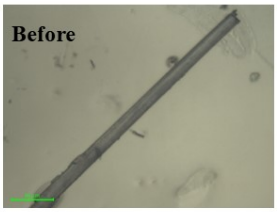

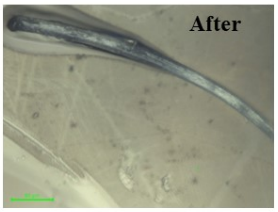

Load/ µN	Modulus /GPa	Hardness/ GPa
775.9512	10.86044	0.70017
718.0948	12.68981	0.590208
562.4395	9.698153	0.463128

Load/ µN	Modulus /GPa	Hardness/ GPa
27.4886	0.224116	0.04833
67.58036	0.543126	0.155956
35.89612	0.306192	0.159558

(b)

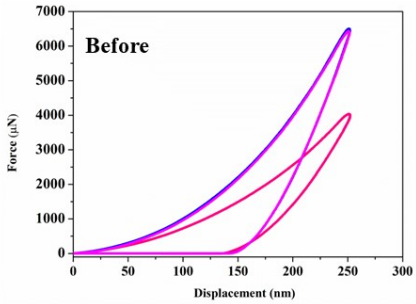

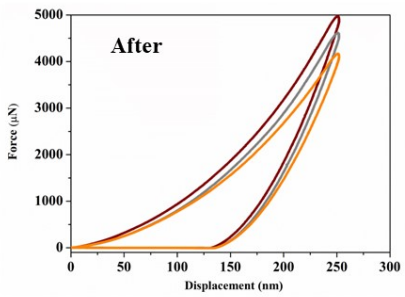

Load/ μN	Modulus /GPa	Hardness/ GPa
3904.619588	50.86718	3.697977
6428.386041	81.95866	6.17696
6366.426516	80.49275	6.160186

Load/ μN	Modulus /GPa	Hardness/ GPa
4499.324	58.11206	4.288253
4833.932	60.82031	4.68811
4052.208	51.91608	3.866918

Figure S18 (a) The modulus and hardness based on nanoindentation before and after irradiation for $B_2(A_{24})_2$; (b) Load-depth (*P-h*) curve for $B_3(A_{24})_2$.

Table S5 Values of *H* (hardness) of various mechanophotonics.

Crystal/Material	Mechanical Property	Hardness (GPa)	Reference
Ethylenediamine salt of *trans*-dichlorocinnamates	**Plastic bending due to photodimerization**	**0.47**	**This work**
1,1′-dioxo-1H,1′H-[2,2′-biindene]-3,3′-diyl-bis-(decanoate) and its polymerised crystal	Elastic to elastic/plastic bending due to photopolymerization with mechanical stiffening	~0.1-~0.3	*J. Am. Chem. Soc.* 2025, **147**, 41034.
1,3-diamino-2,4,5,6-tetrabromobenzene	Elastic bending	0.48	*J. Mater. Chem. C*, 2021, **9**, 9465
N,*N*′-bis(4-nitrophenyl)methanediamine	Elastic or Elasto-plastic bending, ductile frature	0.2	*Chem,* 2024; **10**, 1741.
Isomorphous thiophen-bis(trifluoromethyl)-prop-2-enenitrile	Plastic bending or elastic/plastic bending due to photodimerization	~0.1-~0.2	*Chem. Mater.* 2024, **36**, 8338

d-$B_2(A_{24})_2$

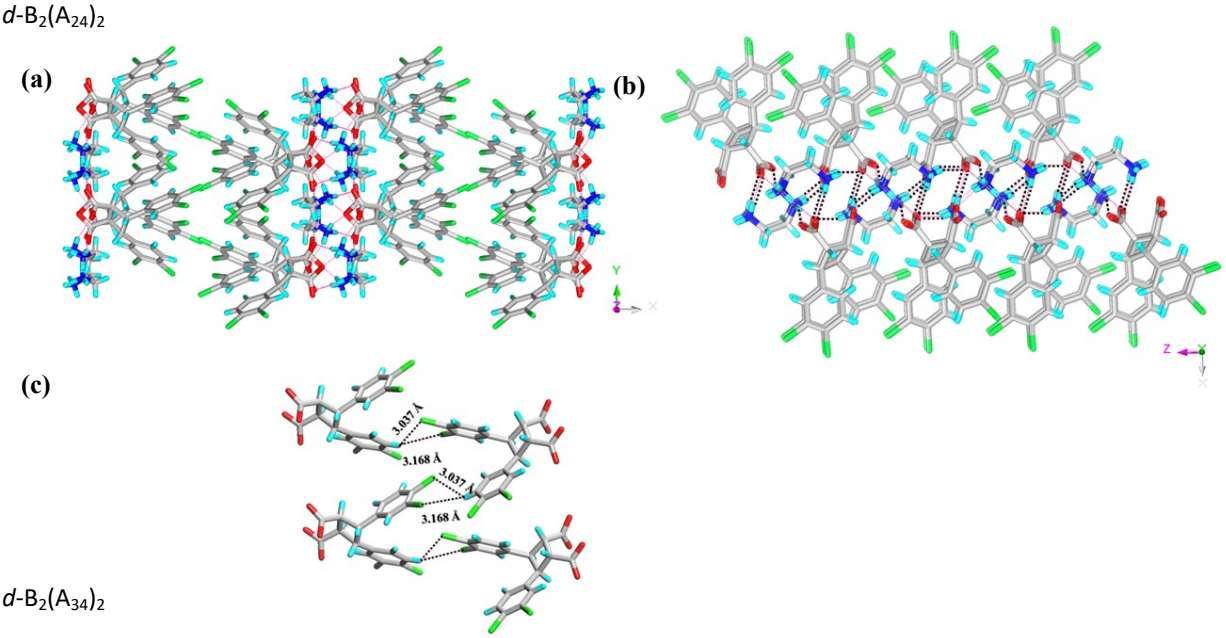

d-$B_2(A_{34})_2$

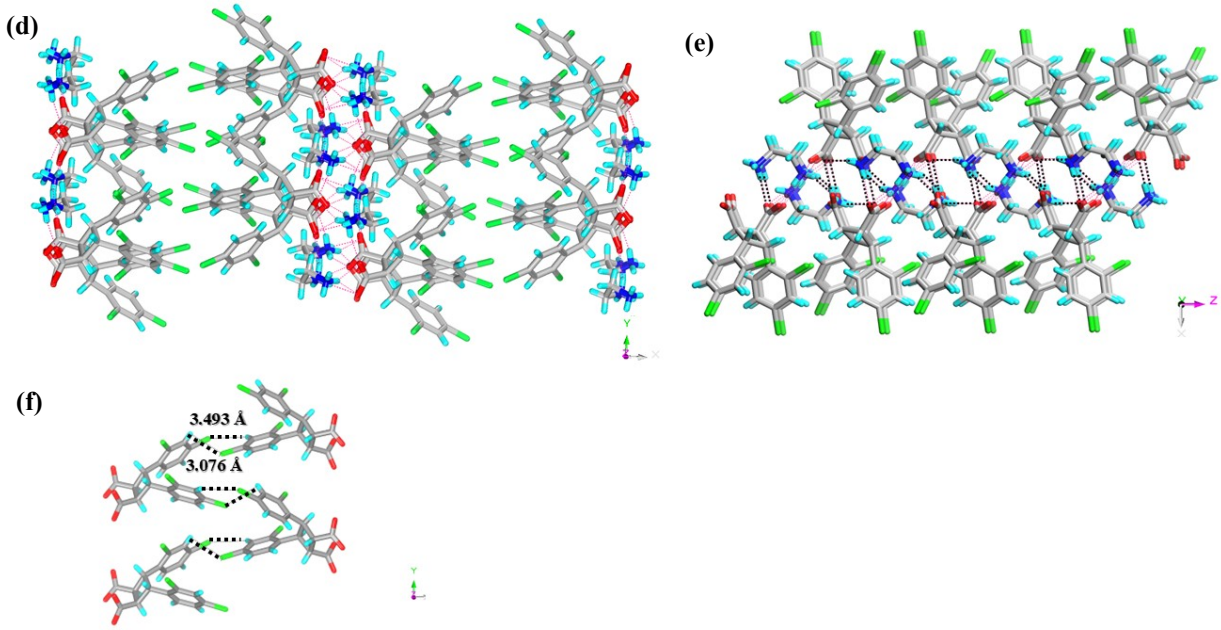

Figure S19 Crystal structure illustration for *d*-$B_2(A_{24})_2$ and *d*-$B_2(A_{34})_2$; (a, d) bilayered 2D hydrogen bonded network (side view), (b, d) top view of 2D HBN, (c, f) C-H···Cl interactions.

PL Spectra

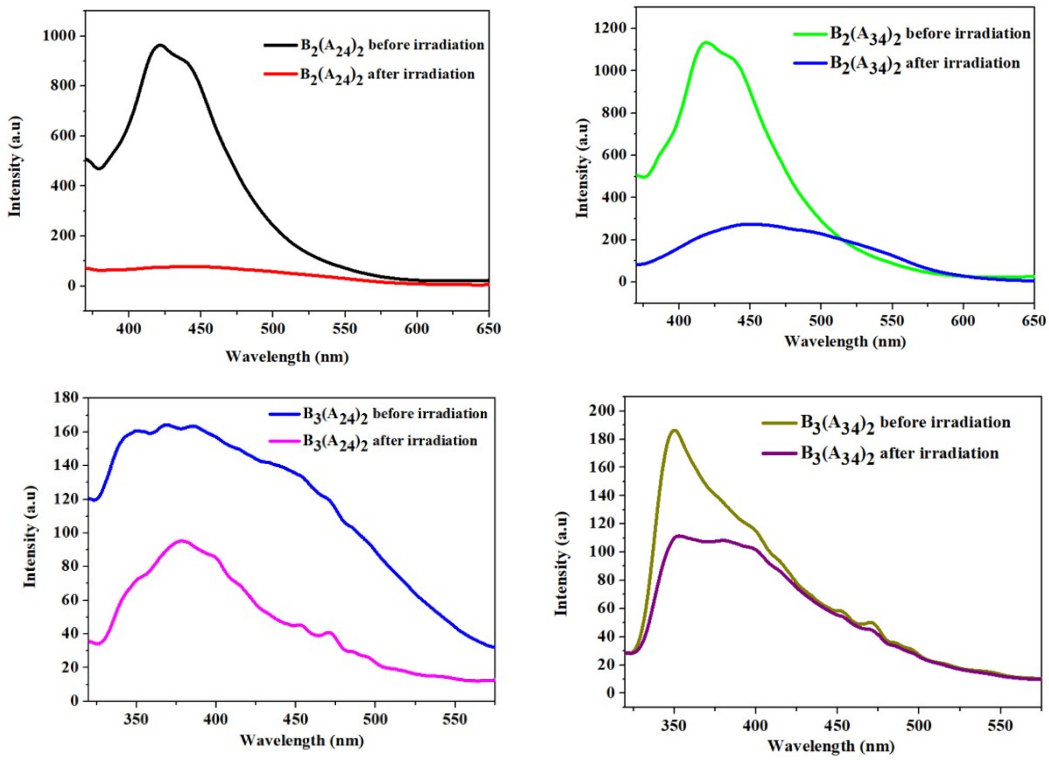

Figure S20 Solid-state PL spectra before and after UV irradiation showing reduced emission.

TGA data after I_2 adsorption.

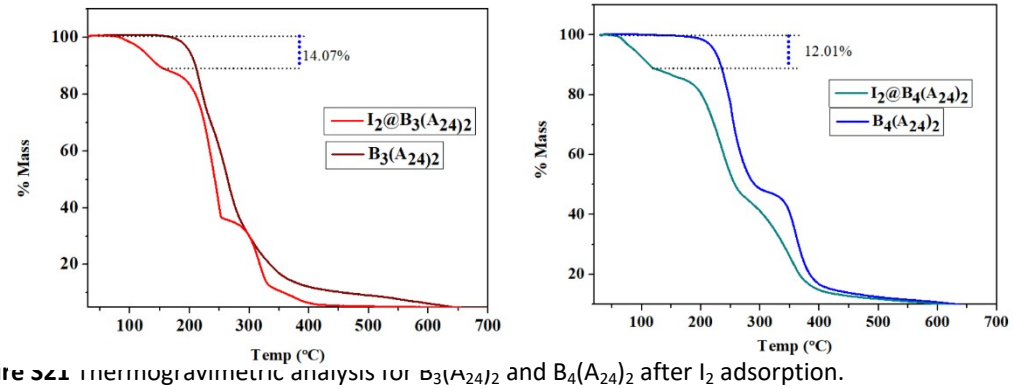

Figure S21 Thermogravimetric analysis for $B_3(A_{24})_2$ and $B_4(A_{24})_2$ after I_2 adsorption.

XPS Spectra

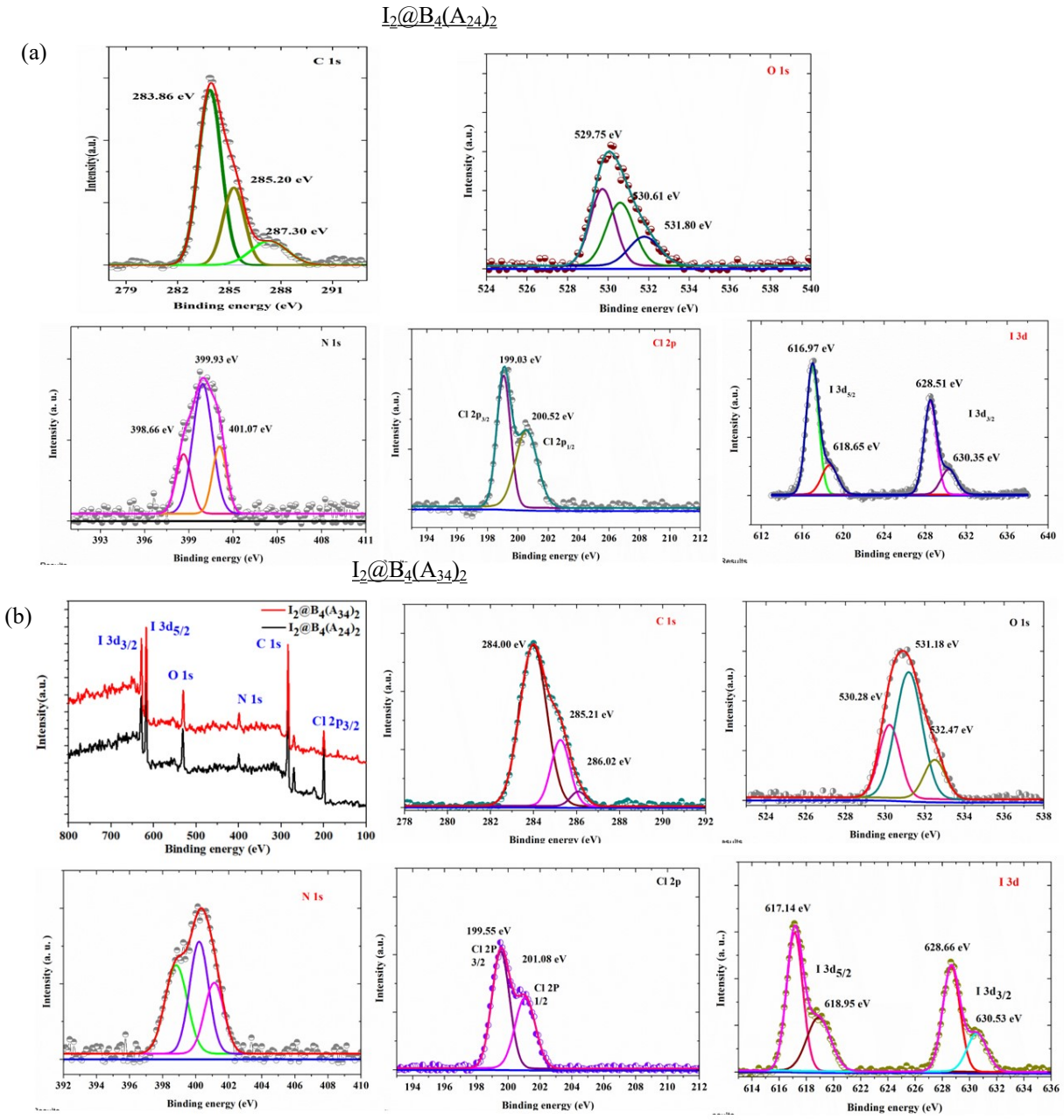

Figure S22 XPS spectra for B_4 salts after I_2 adsorption.

EDX analysis

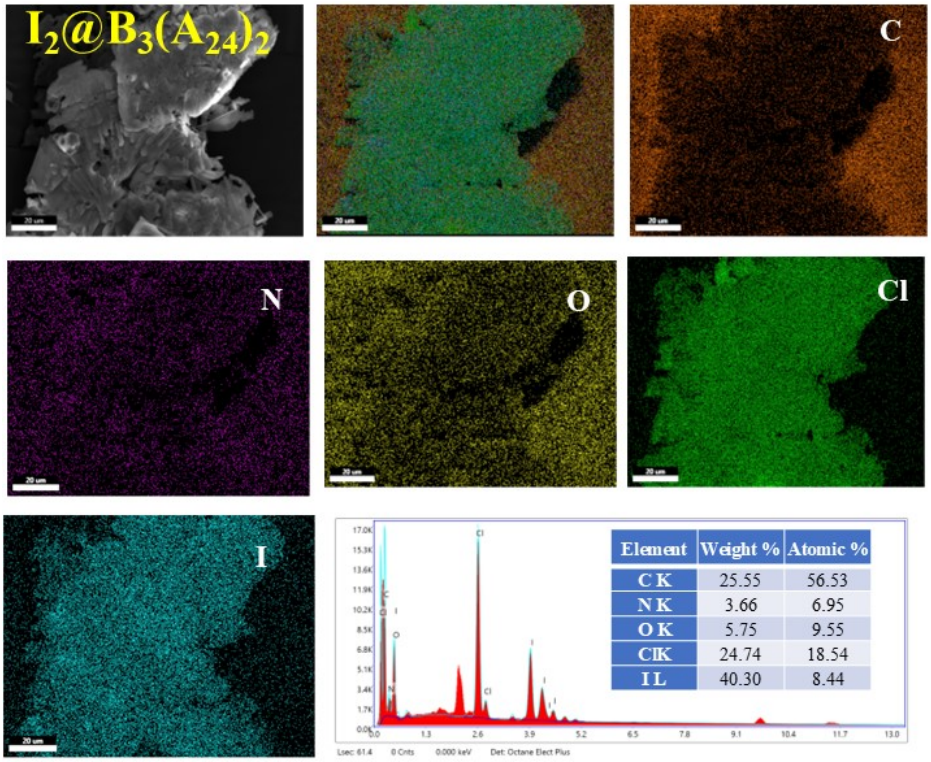

Element	Weight %	Atomic %
C K	25.55	56.53
N K	3.66	6.95
O K	5.75	9.55
Cl K	24.74	18.54
I L	40.30	8.44

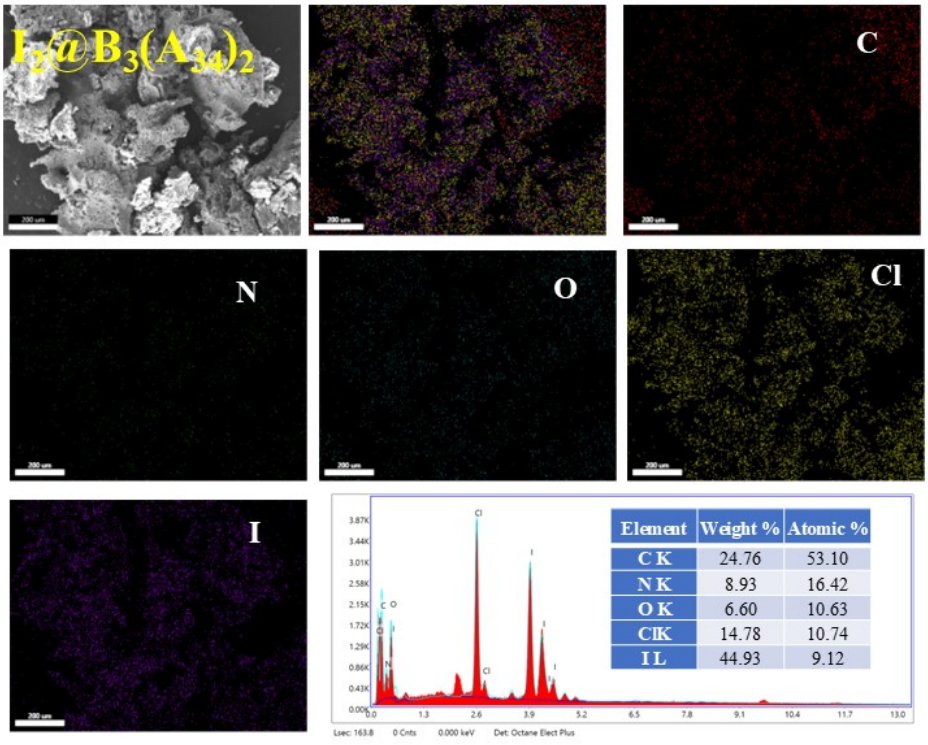

Element	Weight %	Atomic %
C K	24.76	53.10
N K	8.93	16.42
O K	6.60	10.63
Cl K	14.78	10.74
I L	44.93	9.12

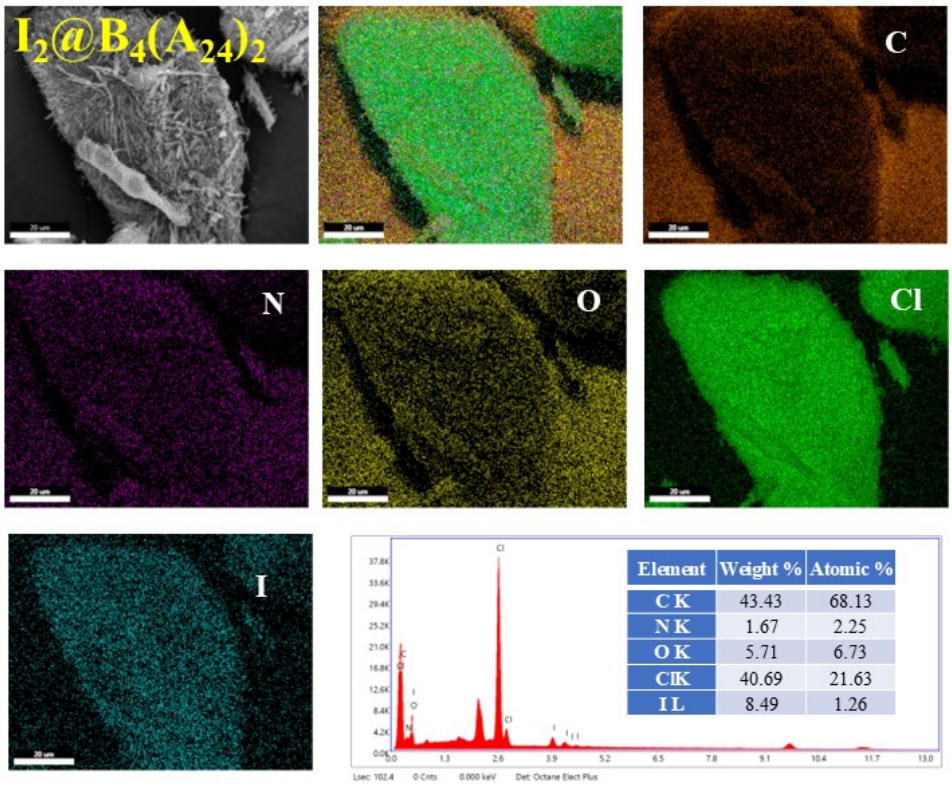

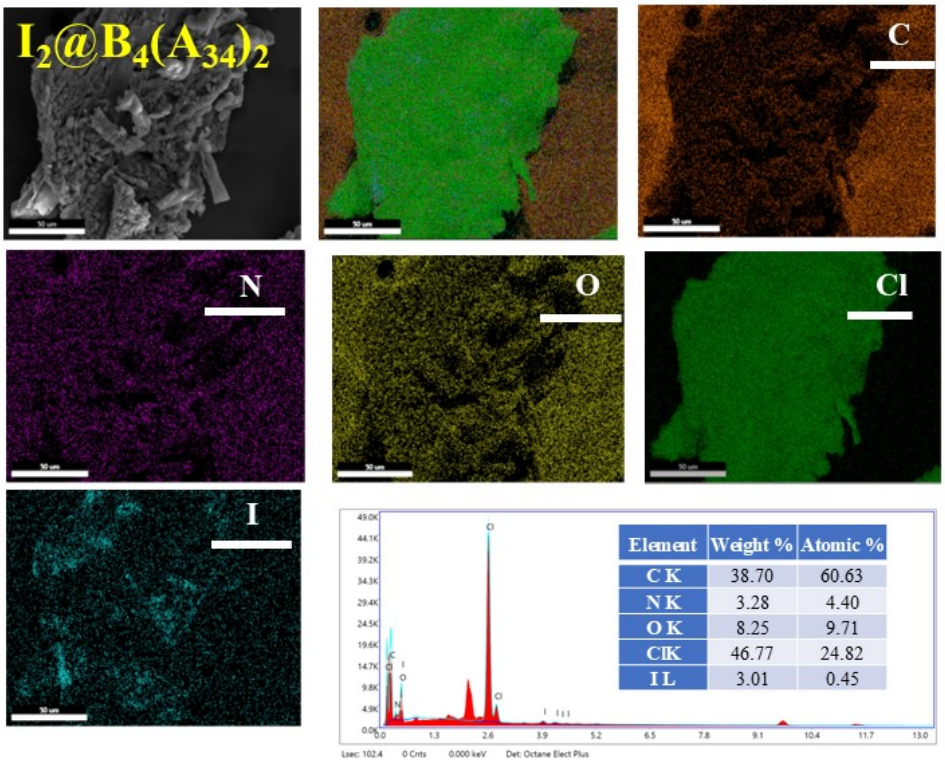

Figure S23 EDX analysis and elemental mapping of different salts after I_2 adsorption.

FTIR Spectra

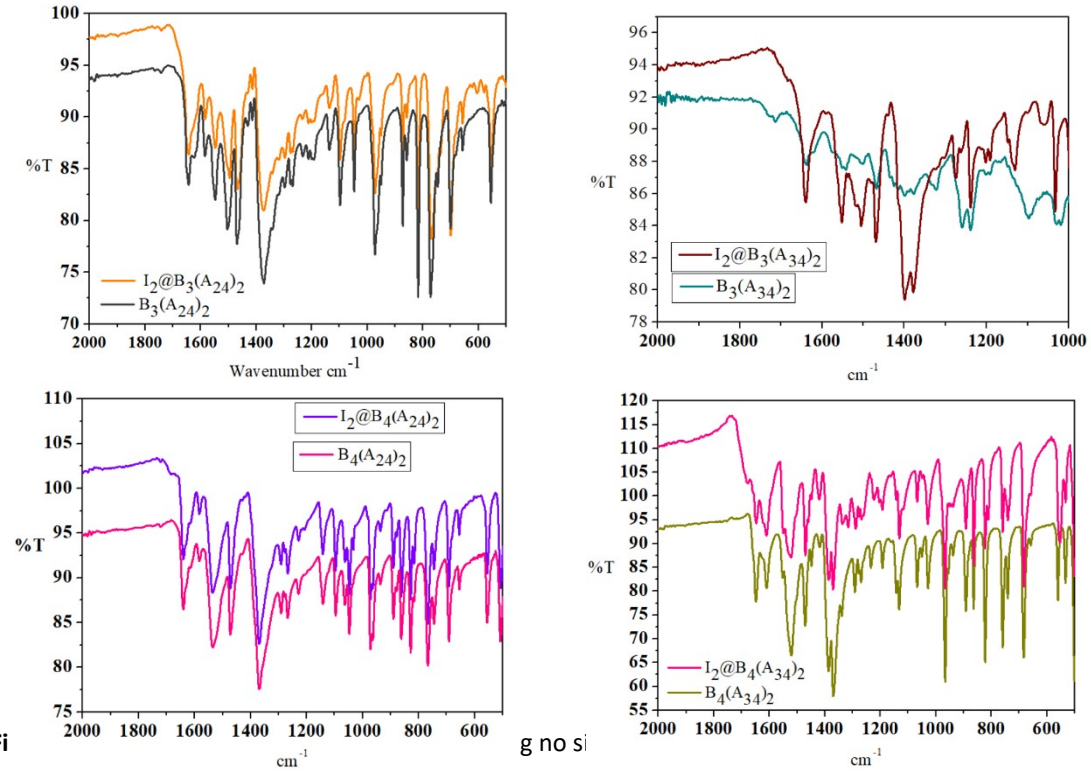

Fi g no si

PXRD analysis after I_2 adsorption

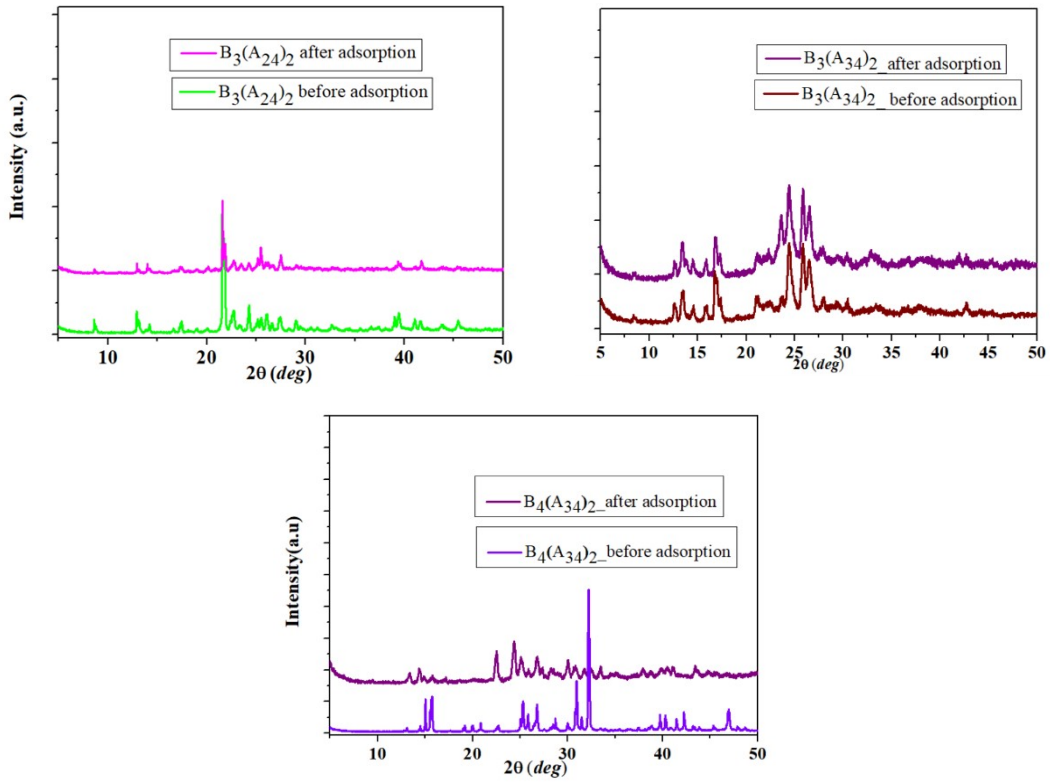

Figure S25 PXRD data showing no significant change in diffraction peak after I_2 adsorption

Raman spectra

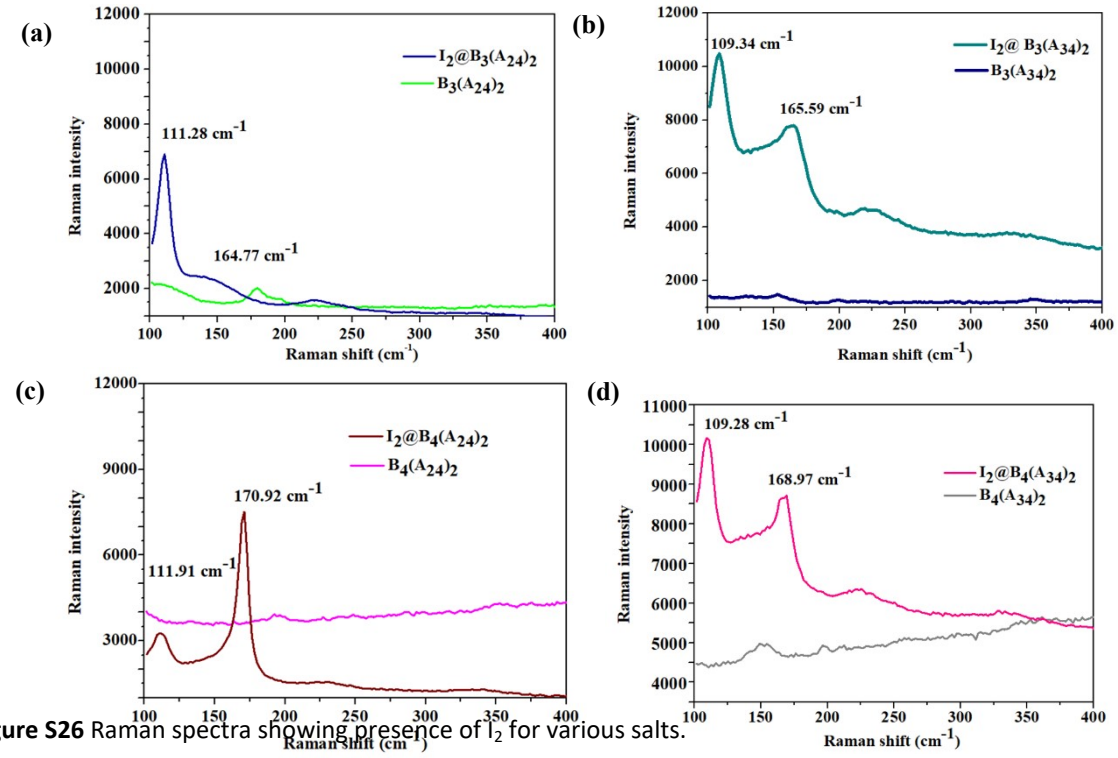

Figure S26 Raman spectra showing presence of I_2 for various salts.

Table S6 I_2 Uptake Capacity of different materials

Name & type of material	**I_2 adsorption phase**	**I_2 adsorption capacity (mg·g^{-1})**	***Ref.***
Simple organic salts of dichlorocinnamic acids with diamines	Vapor phase	330	*This work*
Triazine-based porous organic polymers (NRPOP-1, NRPOP-2)	Iodine in cyclohexane solution	177 and 261	S1
triazene-anthracene-based POP	Iodine in cyclohexane solution	243	S2
Cu-loaded MOF-303	Vapor phase	743 and 837	S3
Unmodified Th-UiO-66	Vapor phase	334	S4
Electron rich POP with imine bonds	Iodine in n-hexane solution	546.1, 594.0 and 489.7	S5

Electrical Conductivity Measurements

The impedance spectroscopy of gel (both aqueous-DMSO and Ph-NO_2 gel) were measured using BioLogic (SP-150e) electrochemical workstation in the frequency range of 0.01 Hz-0.5 MHz. Here, electrical measurement was carried out by dipping two copper plates into the Gel. A white sponge is inserted to the keep the electrode in place during measurement. Distance between plates = 1.5 cm and area covered by the gel is 0.5× 0.5 cm^2.

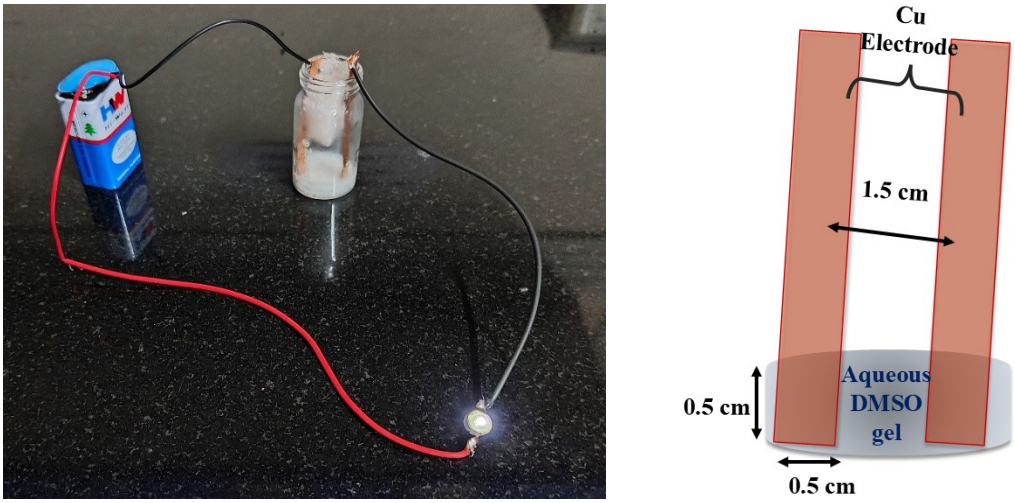

Figure S27 Gel capable of lighting a LED bulb.

The electrical conductivities of the pellets were calculated using the same formula σ = L/(R × A), L is the distance between the two electrodes (here, 0.1 cm), R is the measured resistance, and A is the area of the sample: *i.e.* π $(1)^2$, the diameter of the circular pellet is 1 cm.

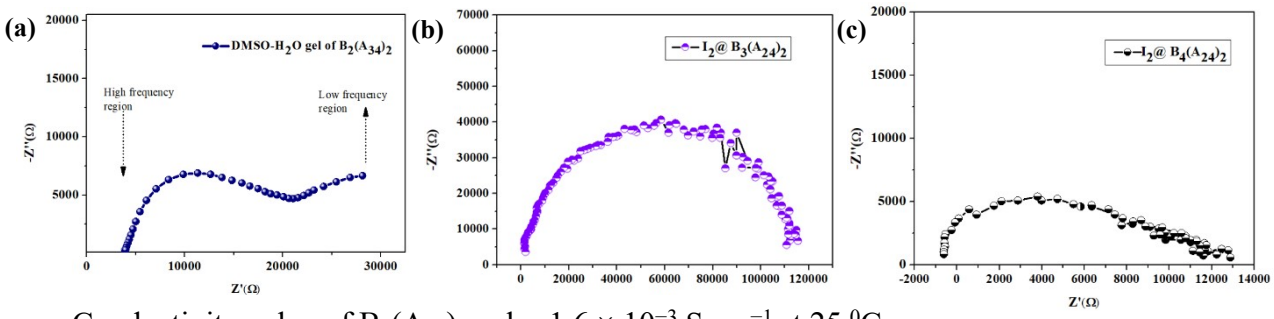

Conductivity value of $B_2(A_{34})_2$ gel = 1.6×10^{-3} S cm^{-1} at 25 ^{0}C

Figure S28 Nyquist spectroscopy plot for aqueous-DMSO gel of $B_2(A_{34})_2$ and I2 adsorbed pellet of $B_3(A_{24})_2$ and $B_4(A_{24})_2$

Reference:

[S1]. A. Mohan, M. H. Al-Sayah, A. Ahmed and O. M. El-Kadri, Triazine-Based Porous Organic Polymers for Reversible Capture of Iodine and Utilization in Antibacterial Application, *Sci. Rep*. 2022, **12**, 2638.

[S2]. M. A. Sabri, M. H. Al-Sayah, S. Sen, T. H. Ibrahim and O. M El-Kadri, Fluorescent Aminal Linked Porous Organic Polymer for Reversible Iodine Capture and Sensing, *Sci. Rep.* 2020, **10**, 15943

[S3]. M. Li, X. Wang, J. Zhang, Y. Gao and W. Zhang, Cu-Loaded MOF-303 for Iodine Adsorption: The Roles of Cu Species and Pyrazole Ligands, *Appl. Surf. Sci.* 2023, **619**, 156819.

[S4]. Z.-J. Li, Y. Ju, H. Lu, X. Wu, X. Yu, Y. Li, X. Wu, Z.-H. Zhang, J. Lin, Y. Qian, M.-Y. He and J.-Q Wang, Boosting the Iodine Adsorption and Radioresistance of Th-UiO-66 MOFs via Aromatic Substitution, *Chem. - Eur. J.* 2021, **27**, 1286–1291.

[S5]. P. Tian, Z. Ai, H. Hu, M. Wang, Y. Li, X. Gao, J. Qian, X. Su, S. Xiao, H. Xu, F. Lu and Y. Gao, Synthesis of Electron-Rich Porous Organic Polymers via Schiff-Base Chemistry for Efficient Iodine Capture, *Molecules* 2022, **27**, 5161.

[S6]. L. Pan, G. Yu, D. Zhai, H. R. Lee, W. Zhao, N. Liu, H. Wang, B. C.-K. Tee, Y. Shi, Y. Cui and Z. Bao, Hierarchical Nanostructured Conducting Polymer Hydrogel with High Electrochemical Activity, *Proc. Natl. Acad. Sci. U. S. A.* 2012, **109**, 9287–9292

[S7]. B. Yao, H. Wang, Q. Zhou, M. Wu, M. Zhang, C. Li, G. Shi, Ultrahigh-Conductivity Polymer Hydrogels with Arbitrary Structures, *Adv. Mater.* 2017, **29**, 1700974

[S8]. Y. Lu, W. He, T. Cao, H. Guo, Y. Zhang, Q. Li, Z. Shao, Y. Cui and X. Zhang, Elastic, Conductive, Polymeric Hydrogels and Sponges, *Sci. Rep.* 2014, **4**, 5792.

[S9]. B. Cao, Q. Tang, L. Li, C.-J. Lee, H. Wang, Y. Zhang, H. Castaneda, G. Cheng, Integrated Zwitterionic Conjugated Poly(Carboxybetaine Thiophene) as a New Biomaterial Platform, *Chem. Sci.* 2015, **6**, 782–788.

[S10]. D. Mawad, E. Stewart, D. L. Officer, T. Romeo, P. Wagner, K. Wagner and G. G. Wallace, Conducting Polymer Hydrogels: A Single Component Conducting Polymer Hydrogel as a Scaffold for Tissue Engineering, *Adv. Funct. Mater.* 2012, **22**, 2691–2691.

[S11]. C. Mahendar, Y. Kumar, M. K. Dixit, M. Mukherjee, A. Kalam and M. Dubey, Conductive Zn(Ii)-Metallohydrogels: The Role of Alkali Metal Cation Size in Gelation, Rheology and Conductance, *Mol. Syst. Des. Eng.* 2021, **6**, 654–661.